JOURNAL OF SYNCHROTRON RADIATION

ISSN 1600-5775

Generalized reverse projection method for grating-based phase tomography

Zhao Wu,[a]* Kun Gao,[a] Zhili Wang,[b] Shengxiang Wang,[c] Peiping Zhu,[c] Yuqi Ren[d] and Yangchao Tian[a]*

[a]National Synchrotron Radiation Laboratory, University of Science and Technology of China, Hefei, Anhui 230029, People's Republic of China, [b]School of Electronic Science and Applied Physics, Hefei University of Technology, Hefei, Anhui 230009, People's Republic of China, [c]Institute of High-Energy Physics, Chinese Academy of Sciences, Beijing 100049, People's Republic of China, and [d]Shanghai Synchrotron Radiation Facility, Chinese Academy of Sciences, Shanghai 201204, People's Republic of China. *Correspondence e-mail: wuzhao@ustc.edu.cn, ychtian@ustc.edu.cn

Received 15 August 2020
Accepted 14 February 2021

Edited by U. Jeng, NSRRC, Taiwan

Keywords: X-ray phase contrast; reverse projection; phase retrieval; computed tomography.

The reverse projection protocol results in fast phase-contrast imaging thanks to its compatibility with conventional computed-tomography scanning. Many researchers have proposed variants. However, all these reverse projection methods in grating-based phase-contrast imaging are built on the hypothesis of the synchronous phase of reference shifting curves in the whole field of view. The hypothesis imposes uniformity and alignment requirements on the gratings, thus the field of view is generally limited. In this paper, a generalized reverse projection method is presented analytically for the case of non-uniform reference in grating-based phase tomography. The method is demonstrated by theoretical derivation, numerical simulations and synchrotron radiation experiments. The influence of imaging position to sensitivity, and the phase-wrapping phenomenon are also discussed. The proposed method combines the advantages of the high efficiency of the reverse projection method and the universal applicability of the phase-stepping method. The authors believe that the method would be used widely in fast and dose-constrained imaging.

1. Introduction

Since the Talbot–Lau interferometer was introduced in X-ray imaging to make the traditional X-ray tube source workable in X-ray grating-based phase-contrast imaging (XGPCI) (Pfeiffer *et al.*, 2006), preclinical applications have been rapidly developed (Bravin *et al.*, 2013; Tapfer *et al.*, 2011, 2012). XGPCI provides multiple complementary images, including phase-contrast and scattering signals, apart from the conventional attenuation signal. The phase-contrast signal represents the refraction angle in radiography and the real part decrement of the X-ray refraction index (equivalent to electron density) in tomography, while the scattering signal reveals the fine structures below the system resolution (Pfeiffer *et al.*, 2008) and medium boundary (Yashiro & Momose, 2015). Thanks to the slower diminution of the real part decrement than that of the imaginary part with increasing imaging energy and/or decreasing atomic number, XGPCI has outstanding advantages in imaging soft tissue in the hard X-ray domain (Bravin *et al.*, 2013; Bech *et al.*, 2009; Tapfer *et al.*, 2011, 2012). The three signals are contained in the acquired raw data, and phase-retrieval protocols become necessary to obtain the separate signals. The phase-stepping (PS) protocol is employed usually to obtain high-quality images. Nevertheless, its discontinuous scanning mode hinders the potential extensive applications of XGPCI, especially in medical

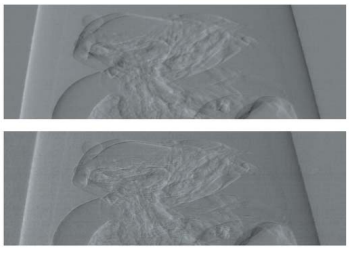

imaging. In this context, many efforts focus on high efficiency and utility phase-retrieval protocols, such as single-shot techniques (Bevins *et al.*, 2012; Momose *et al.*, 2009; Wen *et al.*, 2009; Fu *et al.*, 2019; Ge *et al.*, 2014), the three-image method (Pelliccia *et al.*, 2013), interlaced PS methods (Zanette *et al.*, 2011, 2012), two-shot dark-field imaging (Marschner, Birnbacher *et al.*, 2016), the Moire fringe scanning method (Marschner, Willner *et al.*, 2016), reverse projection methods (Wu *et al.*, 2013; Zhu *et al.*, 2010) as well as its variants including the linear information retrieval method (Wu *et al.*, 2017) and the direct 3D information retrieval method (Wu *et al.*, 2018). Single-shot techniques, the Moire fringe scanning method and reverse projection methods can retrieve information without a grating stepping procedure. Compared with reverse projection methods, single-shot techniques generally have a decreased spatial resolution, while the Moire fringe scanning method is applied to helical computed-tomography scanning.

By extension and sublimation of the relevant work in diffraction-enhanced imaging (Wang *et al.*, 2007), Zhu *et al.* firstly proposed the reverse projection method in 2010 (Zhu *et al.*, 2010), which is considered a simple and fast phase-contrast imaging protocol. Because of its compatibility with conventional computed tomography (CT) scanning, it becomes a hot topic in XGPCI. Thanks to the contributions of many researchers, the reverse projection protocol has been discussed for fan-beam geometry (Wu *et al.*, 2013), two-dimensional imaging configurations (Wang *et al.*, 2012) as well as the case of large refraction angles (Wei *et al.*, 2017), and extended to edge illumination imaging (Hagen *et al.*, 2016). Generally, mutual conjugate front and reverse projections/rays are collected at the half-slope position of the characteristic curves (shifting curve or illumination curve); the attenuation and phase-contrast signals could be retrieved by their combination. But, the condition of half-slope position imaging imposes uniformity and alignment requirements on the gratings. That is why the reverse projection protocol is still limited to small field-of-view (FOV) imaging, after several years of its emergence. The half-slope position is not required in the edge illumination method (Hagen *et al.*, 2016). The authors claimed that non-uniform pre-sample and detector masks were permitted. This is a good idea, but it cannot be realised without considering the difference between front and reverse illumination curves.

Inspired by mention of non-uniform optical elements in edge illumination (Hagen *et al.*, 2016) and calculation of the reference phase-stepping curve (namely shifting curve) in the PS method, we present a generalized reverse projection method analytically in grating-based phase-contrast imaging. The novel method applies to the common case of uneven reference. The framework of its theory is built and its verification by numerical simulations and real experiments is performed. Compared with previous methods, the generalized method does not require collecting images at the half-slope position. Therefore it possesses potential wide applications in the case of large FOV and dose-limitation imaging, such as in biomedical applications (Gromann *et al.*, 2016).

2. Generalized reverse projection method

In grating interferometry, the shifting curve (SC) is a function of the pixel value of the detector versus the relative shift between gratings. It can be obtained experimentally by moving one of the gratings along a direction vertical to the grating lines and optical axis (Momose *et al.*, 2003). Fig. 1 shows fitted experimental reference shifting curves of 102 pixels in a row (20 pixels interval) for six-step PS (see the experimental section below). We find that the shifting curves are generally different among pixels for a centimetre-level FOV. This is caused by non-uniformity and misalignments of the gratings. Under such a condition, the previous reverse projection methods do not work, otherwise the FOV should be reduced further. In consequence, application of the reverse projection protocol for the case of non-uniform reference becomes significant.

Taking the parallel-beam Talbot interferometer as an example, the photon numbers without (subscripts b) or with (subscripts s) sample in the beam path can be expressed by shifting curves as follows where the scattering information is neglected (Wu *et al.*, 2017; Zhu *et al.*, 2010),

$$I_{\rm b}(x, y, \phi) = I_0(x, y)\, S\big(x, y, x_{\rm g}\big), \tag{1}$$

$$I_{\rm s}(x, y, \phi) = I_0(x, y) \exp[-M(x, y, \phi)]\, S\big[x, y, x_{\rm g} + d\theta(x, y, \phi)\big], \tag{2}$$

where I_0 is the incident photon number per pixel without gratings and sample in the beam path, $S(x, y, x_{\rm g})$ denotes the normalized SC at pixel (x, y) with argument of relative transverse shift $x_{\rm g}$ between gratings along the x direction, $M(x, y)$ and $\theta(x, y)$ express the attenuation signal and the refraction angle, respectively, d represents the distance between gratings, and ϕ is the view angle in tomography.

Performing a circular scanning, front and reverse projections can be obtained. On account of the same attenuation and opposite refraction angle between the front and reverse projections, the following formulae are obtained when the

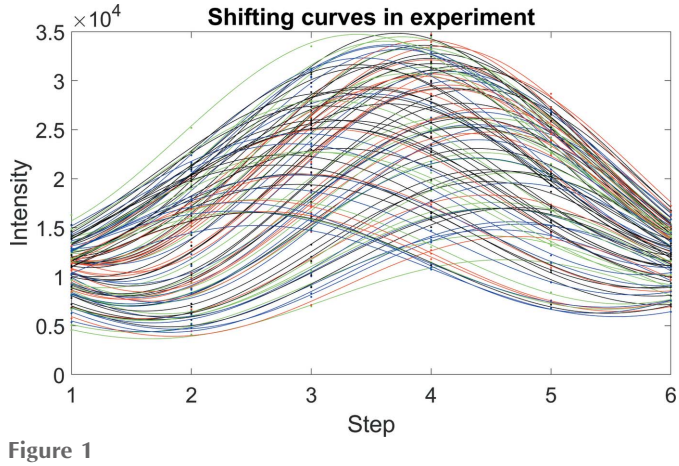

Figure 1
Fitted reference shifting curves of 102 pixels in a row for six-step PS (see Section 3.2).

grating is located at x_g^0 according to equation (2) (Zhu *et al.*, 2010),

$$I_s(x, y, \phi) = I_0(x, y) \exp[-M(x, y, \phi)] \times S\left[x, y, x_g^0 + d\theta(x, y, \phi)\right], \quad (3)$$

$$I_s(-x, y, \phi + \pi) = I_0(-x, y) \exp[-M(x, y, \phi)] \times S\left[-x, y, x_g^0 - d\theta(x, y, \phi)\right]. \quad (4)$$

The schematic diagram shown in Fig. 2 displays the relationship visually. Generally, the photon number in each pixel can be well approximated as a cosine function (Bravin *et al.*, 2013; Chen *et al.*, 2011; David *et al.*, 2002; Yashiro & Momose, 2015; Wu *et al.*, 2015),

$$I_b(x, y) = a(x, y) + a(x, y)\, V_0(x, y) \cos\left[2\pi \frac{x_g^0}{p_2} + \varphi(x, y)\right], \quad (5)$$

where $a(x, y)$, $V_0(x, y)$ and $\varphi(x, y)$ stand for the averaged intensity, visibility and initial phase of the reference shifting curve, respectively, and p_2 is the pitch of the analyzer grating. For simplicity, the coordinate parameters in brackets are omitted in the following derivations, $I_F = I_s(x, y, \phi)$, $I_R = I_s(-x, y, \phi + \pi)$, $a_F = a(x, y)$, $a_R = a(-x, y)$, $V_F = V_0(x, y)$, $V_R = V_0(-x, y)$, $\varphi_F = \varphi(x, y)$, $\varphi_R = \varphi(-x, y)$, where subscripts F and R stand for front and reverse, respectively. Based on the cosine model, we can rewrite equations (3) and (4) as

$$I_F = a_F \exp(-M)\left[1 + V_F \cos\left(2\pi \frac{x_g^0 + d\theta}{p_2} + \varphi_F\right)\right], \quad (6)$$

$$I_R = a_R \exp(-M)\left[1 + V_R \cos\left(2\pi \frac{x_g^0 - d\theta}{p_2} + \varphi_R\right)\right]. \quad (7)$$

It is noteworthy that the front and reverse projections are not always mutually conjugate in the case under consideration. The formula below can be derived from equation (6) divided by equation (7),

$$T = \frac{I_F}{I_R} = a_F\left[1 + V_F \cos\left(2\pi \frac{x_g^0 + d\theta}{p_2} + \varphi_F\right)\right] \Big/ a_R\left[1 + V_R \cos\left(2\pi \frac{x_g^0 - d\theta}{p_2} + \varphi_R\right)\right]. \quad (8)$$

Defining the following equations,

$$A_{F/R} = a_{F/R} V_{F/R} \cos\left(2\pi \frac{x_g^0}{p_2} + \varphi_{F/R}\right), \quad (9)$$

$$B_{F/R} = a_{F/R} V_{F/R} \sin\left(2\pi \frac{x_g^0}{p_2} + \varphi_{F/R}\right), \quad (10)$$

$$\cos(\beta) = \frac{A_F - TA_R}{\left[(A_F - TA_R)^2 + (B_F + TB_R)^2\right]^{1/2}}, \quad (11)$$

$$\sin(\beta) = \frac{B_F + TB_R}{\left[(A_F - TA_R)^2 + (B_F + TB_R)^2\right]^{1/2}}, \quad (12)$$

$$\cos(\gamma) = \frac{-a_F + Ta_R}{\left[(A_F - TA_R)^2 + (B_F + TB_R)^2\right]^{1/2}}, \quad (13)$$

when $A_F - TA_R \neq 0$ or $B_F + TB_R \neq 0$,

$$\cos\left(\frac{2\pi d}{p_2}\theta + \beta\right) = \cos(\gamma). \quad (14)$$

Refer to the Appendix *A* for derivation of equation (14), which is a critical result of the generalized reverse projection method. β mainly relies on the relative shift x_g^0 between gratings (called the 'imaging position' hereon) and the initial phases of front and reverse reference SCs. It can be considered approximately as the phase of the imaging position, even though it is related to the ratio T of the front projection to the reverse projection. γ is the final phase resulting from refraction of the sample. A is the offset intensity at the imaging position relative to the averaged intensity of the shifting curve. We find that the retrieved angle range, depending on the value of β, is limited by the injective part of the cosine function. When $\beta = k\pi - \pi/2$, $k \in Z$, the sensitivity is high and the retrieval ranges of the plus and minus angle are symmetric. On the contrary, low sensi-

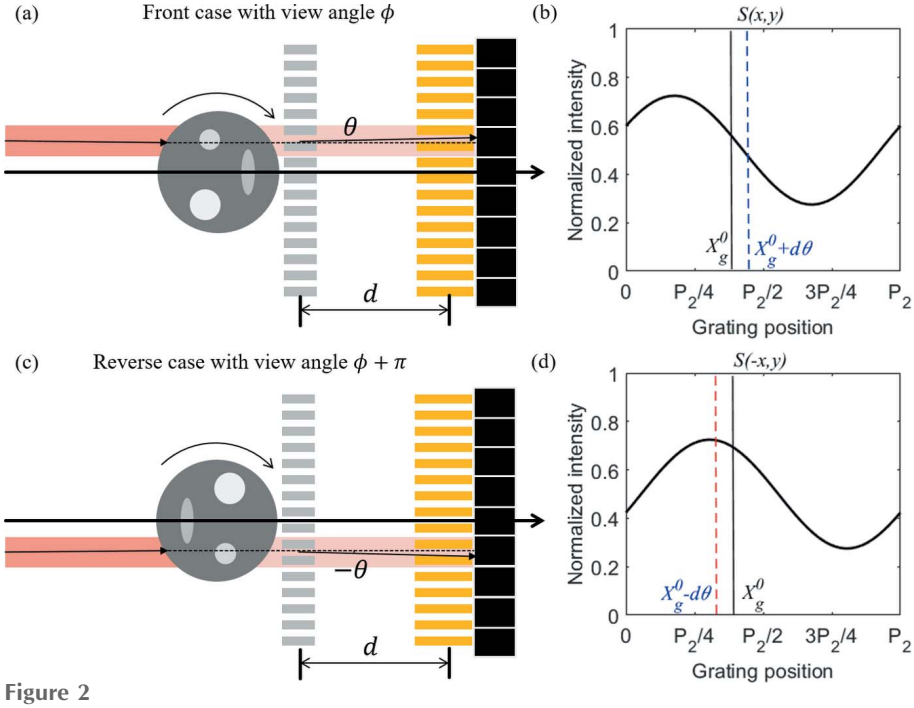

Figure 2
Schematic diagram of the generalized reverse projection method: thick black arrows go through rotation axes and denote the optic axes. Front and reverse projections are collected under different shifting curves (hereinafter referred to as 'front and reverse shifting curves'). The deflection of the ray in one pixel can be observed by the interferometer and retrieved from the front and reverse projections.

Table 1
Expressions of equation (14) under different conditions.

Conditions	Expressions
$A_F - TA_R > 0 \cap \beta_0 \geq 0$	$\cos(2\pi d\theta/p_2 + \beta_0) = \cos(\gamma_0)$
$A_F - TA_R > 0 \cap \beta_0 < 0$	$\cos(2\pi d\theta/p_2 + \beta_0) = \cos(-\gamma_0)$
$A_F - TA_R < 0 \cap \beta_0 \geq 0$	$\cos(2\pi d\theta/p_2 + \beta_0 - \pi) = \cos(-\gamma_0)$
$A_F - TA_R < 0 \cap \beta_0 < 0$	$\cos(2\pi d\theta/p_2 + \beta_0 + \pi) = \cos(\gamma_0)$

tivity and phase wrapping (Epple *et al.*, 2015) emerge easily for $\beta \simeq k\pi$. Due to different retrieval mechanisms, the phase-wrapping phenomenon in the proposed method is totally different from that in the PS method. When more than half of a Moire fringe exists in the FOV, the opposite slopes of the front and reverse SCs at the imaging position result in $\beta_0 = 0$ in some pixels. This is a main drawback of the proposed method. With the development of grating manufacture technology, we believe this drawback can be weakened and ignored. Fortunately, the reverse projection method generally has a higher sensitivity, which is more important than the measurement range, according to Wu *et al.* (2015). In that sense, the proposed method may be more suitable to high-energy imaging.

As $A_F - TA_R \neq 0$, we define $\beta_0 = \tan^{-1}[(B_F + TB_R)/(A_F - TA_R)]$. Considering the small refraction angle in real phase contrast imaging, equation (14) can be expressed in different forms in the four conditions shown in Table 1, with the definition $\gamma_0 = \cos^{-1}\{(-a_F + Ta_R)/[(A_F - TA_R)^2 + (B_F + TB_R)^2]^{1/2}\}$.

From Table 1, the refraction angle can be retrieved by the following equations,

$$\theta_{retr} = \begin{cases} \frac{p_2}{2\pi d}(\gamma_0 - \beta_0) & A_F - TA_R > 0 \quad and \quad \beta_0 \geq 0, \\ \frac{p_2}{2\pi d}(-\gamma_0 - \beta_0) & A_F - TA_R > 0 \quad and \quad \beta_0 < 0, \\ \frac{p_2}{2\pi d}(\pi - \gamma_0 - \beta_0) & A_F - TA_R < 0 \quad and \quad \beta_0 \geq 0, \\ \frac{p_2}{2\pi d}(-\pi + \gamma_0 - \beta_0) & A_F - TA_R < 0 \quad and \quad \beta_0 < 0. \end{cases} \tag{15}$$

The phase wrapping emerges for $\beta_0 = 0$ even with small refraction angle, when $(2\pi d\theta/p_2 + \beta_0)\beta_0 < 0$.

As $A_F - TA_R = 0$ and $B_F + TB_R \neq 0$, the retrieval formula from equation (14) becomes

$$\theta_{retr} = -\frac{p_2}{2\pi d}\ \sin^{-1}\left(\frac{-a_F + Ta_R}{B_F + TB_R}\right). \tag{16}$$

Along with the formulae of the refraction angle, the attenuation signal can be retrieved by equation (17) on the basis of equations (6) and (7),

$$M_{retr} = -\ln\left(\frac{I_F + I_R}{C + D}\right), \tag{17}$$

where

$$C = a_F + a_F V_F \cos\left(2\pi\frac{x_g^0 + d\theta_{retr}}{p_2} + \varphi_F\right), \tag{18}$$

$$D = a_R + a_R V_R \cos\left(2\pi\frac{x_g^0 - d\theta_{retr}}{p_2} + \varphi_R\right). \tag{19}$$

In the previous reverse projection methods, many steps need to be collected to obtain accurate fitted reference SCs. Thanks to the cosine model, only several steps need to be collected in the presented method, which is similar to the procedure of the PS method. Replacing x_g^0 by np_2/N, the reference SC in equation (5) is denoted as I_{bn} $(1 \leq n \leq N)$. When the sample is imaged at the position of the n_0th step, a_F, A_F and B_F can be calculated according to the formulae below (Wu *et al.*, 2015),

$$a_F = \frac{1}{N}\sum_{n=1}^{N} I_{bn}, \tag{20}$$

$$A_F = \frac{2}{N}\sum_{n=1}^{N} I_{bn}\cos\left(2\pi\frac{n - n_0}{N}\right), \tag{21}$$

$$B_F = -\frac{2}{N}\sum_{n=1}^{N} I_{bn}\sin\left(2\pi\frac{n - n_0}{N}\right). \tag{22}$$

In a special case of $a_F = a_R = a$, $V_F = V_R = V_0$, $\varphi_F = \varphi_R = 0$, $x_g^0 = -p_2/4$, which was mainly discussed in the previous reported publications, the retrieval formulae of the refraction angle and attenuation signal are simplified from equations (16) and (17) to be

$$\theta_{retr} = \frac{p_2}{2\pi d}\ \sin^{-1}\left[\frac{I_F - I_R}{V_0(I_F + I_R)}\right], \tag{23}$$

$$M_{retr} = -\ln\left(\frac{I_F + I_R}{2a}\right), \tag{24}$$

which are in good accordance with the reported results (Li *et al.*, 2016).

In the case of $A_F - TA_R = 0$ and $B_F + TB_R = 0$, T remains a constant with changing refraction angle and attenuation signal, thus the signals cannot be retrieved.

3. Results and discussion

Numerical simulations and synchrotron radiation experiments have been performed using a Talbot interferometer with non-uniform reference, in order to investigate the feasibility and validity of the established novel phase-contrast imaging approach.

3.1. Simulated results

According to the reported parameters of the Shanghai Synchrotron Radiation Facility (SSRF) (Xi *et al.*, 2012), an absorption grating with a period of 2.4 µm is located at the first-order fractional Talbot distance of a $\pi/2$ phase-shift grating with a period of 2.396 µm. The imaging energy was set at 20 keV and the pixel size of the detector was 13 µm. A Shepp–Logan phantom of the same composition as in Wu *et al.* (2013) was designed as the sample and immersed in water. Its size was 6.5 mm × 6.5 mm. We emulated the case where one-quarter of the Moire fringe was covering the FOV, and

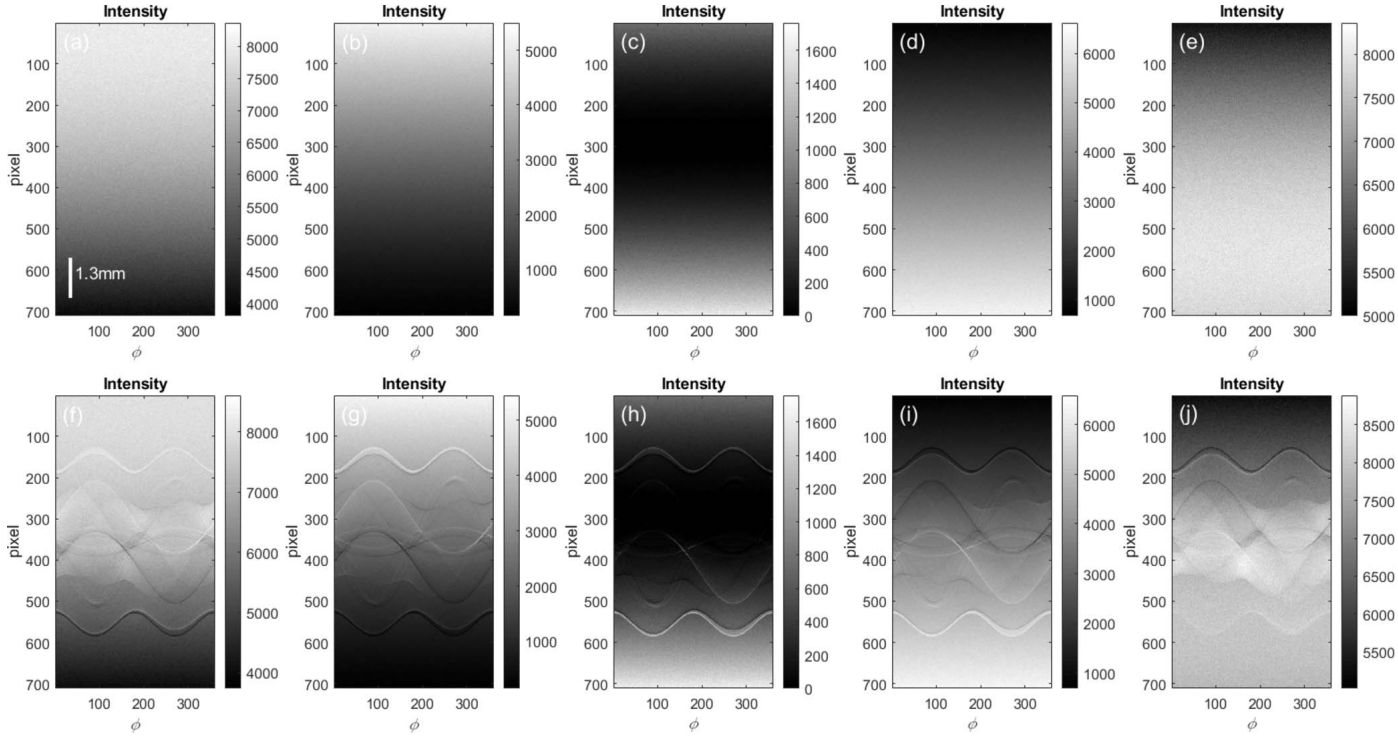

Figure 3
Five reference (*a*–*e*) and sample (*f*–*j*) sinograms at each step in the PS method when one-quarter of the Moire fringe covers the FOV.

considered the incident photon number of 50000 at one step and a visibility of 40% for the established method. We also simulated a five-step PS with 10000 photons at each step to perform a comparison under the same total illumination intensity. Both datasets were collected at 360 viewing angles evenly distributed over the whole circumference. A Poisson noise model was employed in the data collection procedure.

Fig. 3 shows sinograms of the reference and sample images using the PS method with one-quarter of the Moire fringe in the FOV. The counterparts of the retrieved information by the presented method are displayed in Fig. 4. The corresponding slices, reconstructed by filtered back-projection method (Huang *et al.*, 2006; Pfeiffer *et al.*, 2007), are shown in Fig. 5. All the retrieved information and reconstructed slices are identical, except for the noise level or sensitivity. This is caused by the distribution of β in equation (14), which has been discussed in Section 2. Fig. 6 presents images of β_0 and their distribution histograms at each step, from which we can see that the values of β_0 at the third step are close to zero radians. That is why the retrieved information in Figs. 4(*c*) and 4(*h*) and the reconstructed slices in Figs. 5(*c*) and 5(*h*) are inferior.

The results by the PS method were also calculated to compare with the results at the fifth step (the best one) by the presented method in Fig. 7. Comparisons of the profiles of the reconstructed phase and absorption slices are shown in panels (*i*) and (*j*). The good agreement with the PS method proved the feasibility and veracity of the novel method in the case of non-uniform reference.

3.2. Experimental results

The experiment was carried out at SSRF BL13W1, whose system parameters were the same as those in the simulations except for a pixel size of 6.5 µm. We performed imaging of a biological sample, a bee, in the designed scanning mode. First, conventional phase-contrast tomography was performed, with a six-step PS and 360 viewing angles evenly distributed around a semi-circumference. Then, we collected the data at the third step and 720 viewing angles evenly distributed over the whole circumference.

Maps of averaged intensity, visibility and initial phase of SCs are shown in Fig. 8, from which we can see the difference among the SCs. In particular, there is more than a $\pi/2$ phase variation in panel (*c*). Figs. 9(*a*)–9(*d*) show absorption images and phase images of the bee at the first tomographic viewing angle, retrieved by the PS method and the proposed method, respectively. Profile comparisons are also shown in Figs. 9(*e*)–9(*f*); their consistency proved the feasibility of the presented phase-contrast imaging approach for the common case of uneven reference. We also carried out phase-contrast computed tomography (PCCT) employing the two methods; the results and comparisons presented in Fig. 10 confirm the applicability of the proposed method to three-dimensional biomedical imaging. It is worth noting that the exposure time and thus radiation dose to sample in our method is only one-third of those used in the PS method.

Images of comparable quality were obtained using the proposed method, although the exposure time was one-third

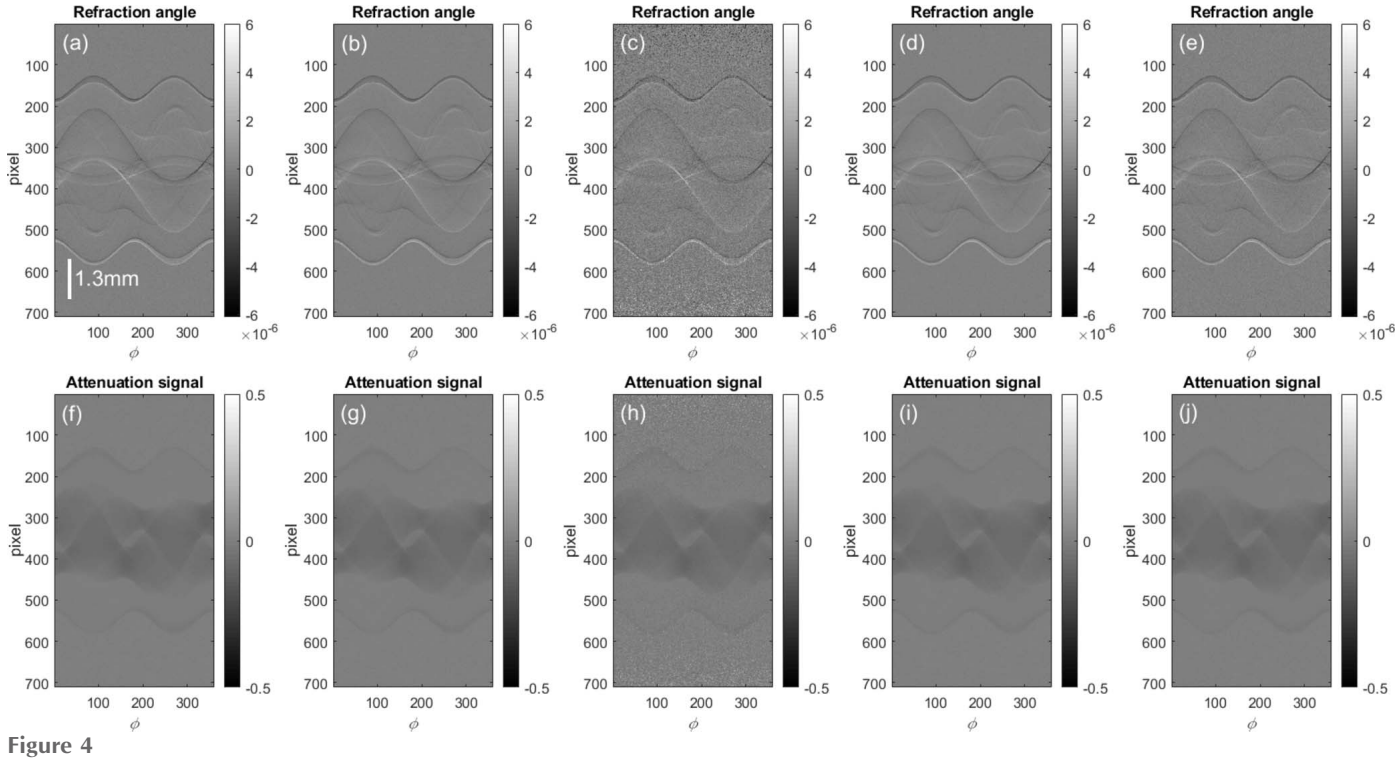

Figure 4
Phase retrieval by the proposed method at different steps: (*a*–*e*) sinograms of the extracted refraction angle, (*f*–*j*) sinograms of the extracted attenuation.

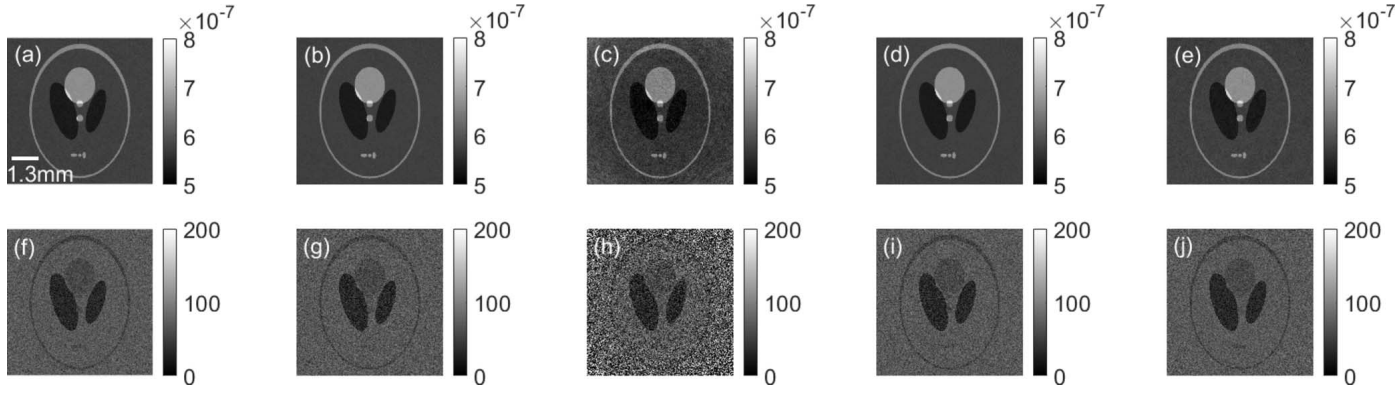

Figure 5
Reconstructed slices of the real part decrement of the refraction index (*a*–*e*) and attenuation coefficient (*f*–*j*) by the proposed method at different steps.

of that of the conventional PS method. Compared with the PS method, the presented method is more sensitive to the instability of the shifting curve. The tiny difference may be caused by slowly drifting illumination light. Furthermore, the verticality between the rotation axis and the row direction of the detector also influenced the accuracy of the extracted information by the new method. The imaging results may be improved by collecting reference SCs several times or (and) aligning the axis precisely.

At SSRF, the imaging geometry is parallel beam, the collection program controls the motor rotating only half-circle automatically in CT collection mode. However, the proposed method needs whole circular scanning for phase tomography. PCCT by the proposed method was completed by two half-circle scanning, and the raw datasets in PCCT of the two methods were collected respectively. This may be another reason for the tiny difference between the two methods in the experiments. Although we only discussed the proposed method in parallel beam geometry, its applications in unparallel beam geometry are available according to the ideas reported by Wu *et al.* (2013).

4. Conclusion

In this report, we established and discussed a generalized reverse projection method analytically in grating-based phase tomography. The dependency relationship between the imaging performance and the imaging position was also revealed and discussed. Numerical simulations and real experiments have been performed to support its validity and

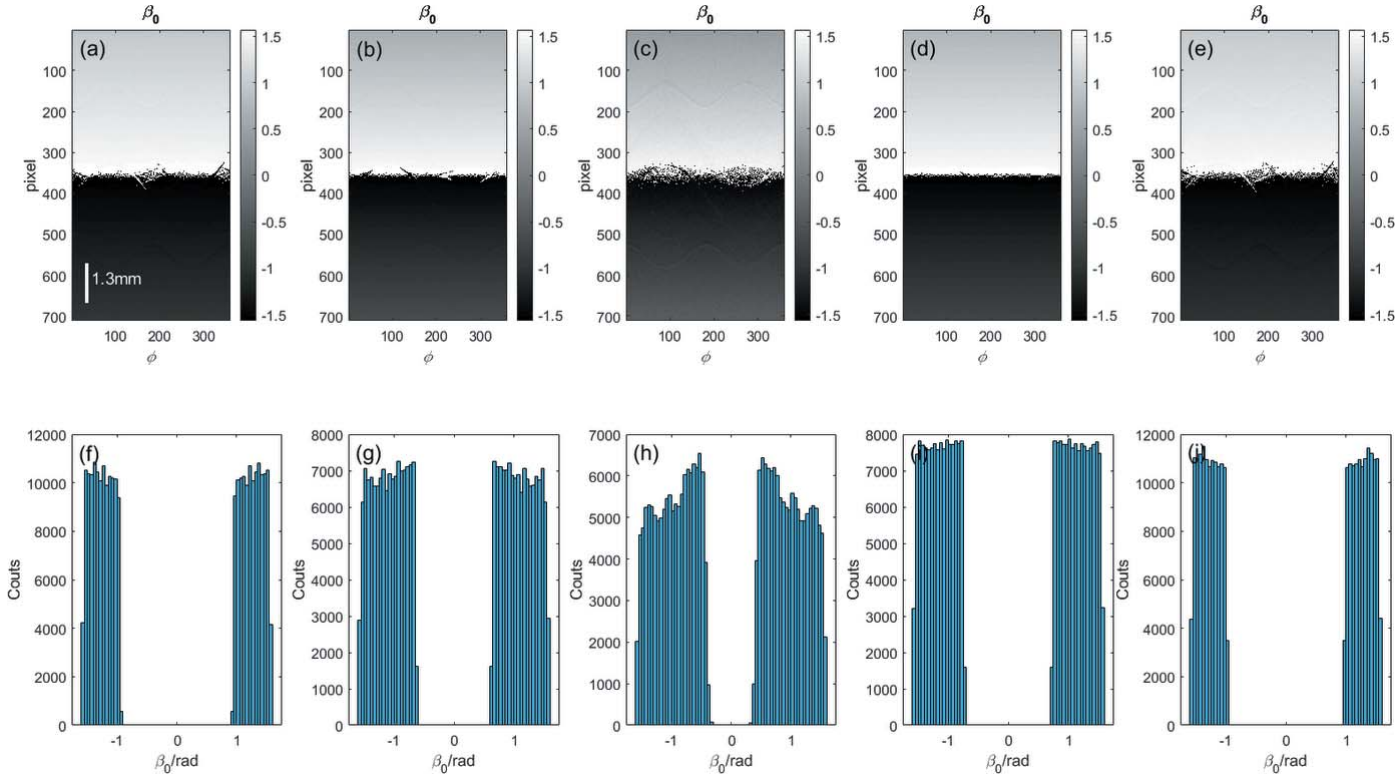

Figure 6
Images of β_0 (*a*–*e*) and their distribution histograms (*f*–*j*) at different steps.

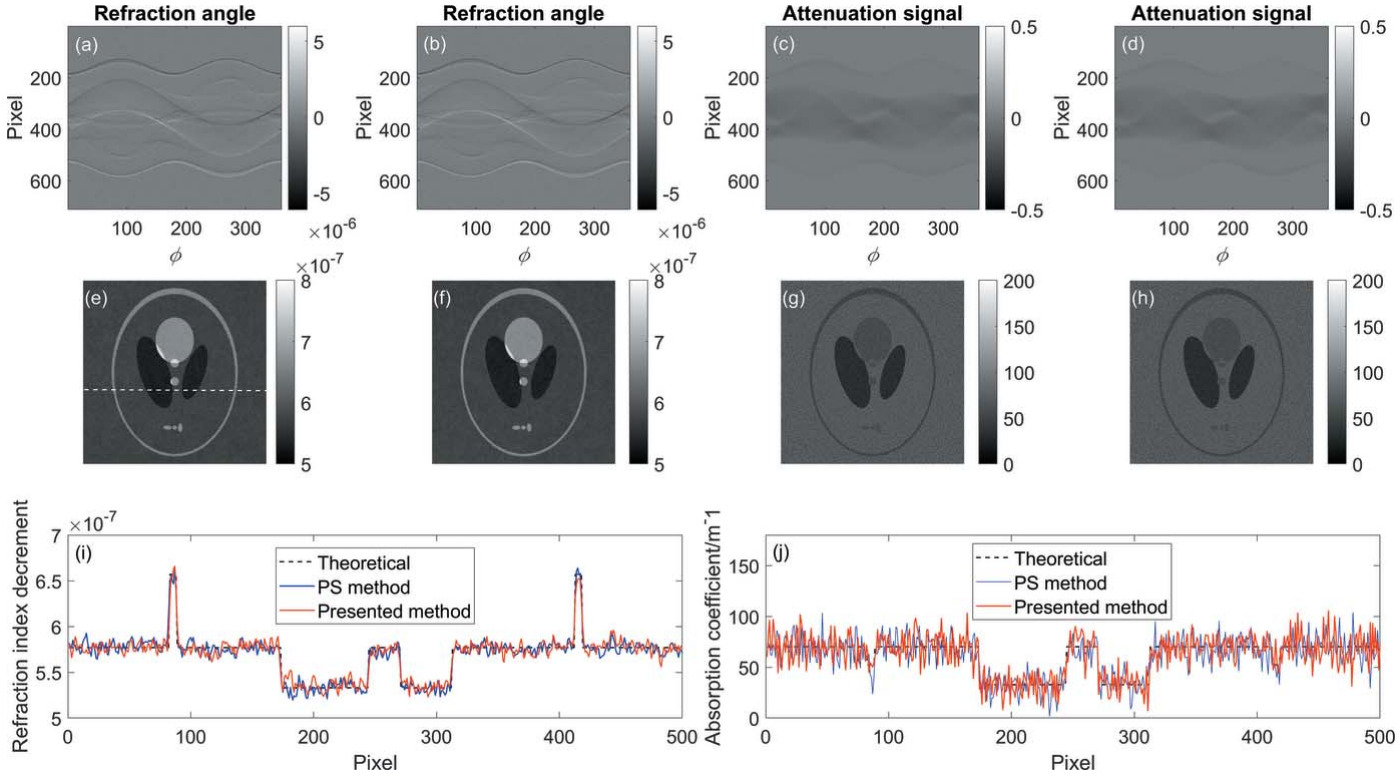

Figure 7
Comparison of results by the PS method (*a*, *c*, *e* and *g*) and the proposed method (*b*, *d*, *f* and *h*): sinograms of the extracted refraction angle (*a*–*b*), sinograms of the extracted absorption (*c*–*d*), reconstructed phase slices (*e*–*f*) and absorption slices (*g*–*h*). Profile comparison of slices at the position of the white dotted line in (*e*) are shown in panels (*i*) (phase) and (*j*) (absorption).

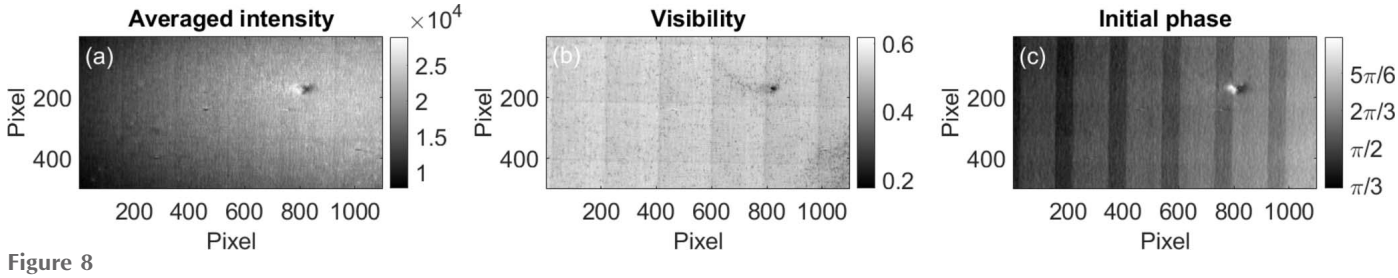

Figure 8
Maps of averaged intensity (*a*), visibility (*b*) and initial phase (*c*) of the reference shifting curve in the whole FOV.

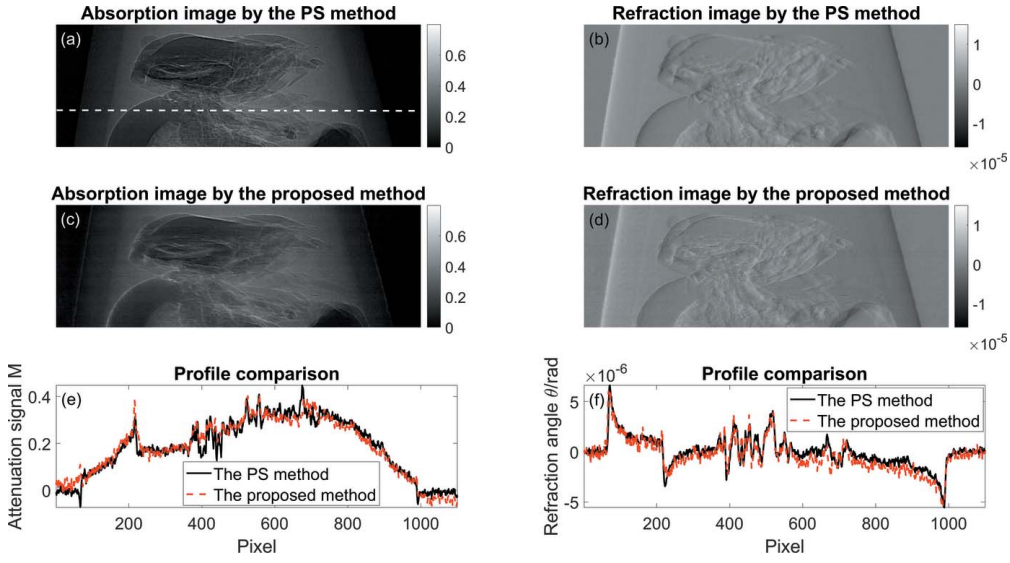

Figure 9
Retrieved absorption images and phase images of a bee by (*a*–*b*) the PS method and (*c*–*d*) the proposed method, as well as (*e*–*f*) their profiles comparison as the white dotted line in panel (*a*).

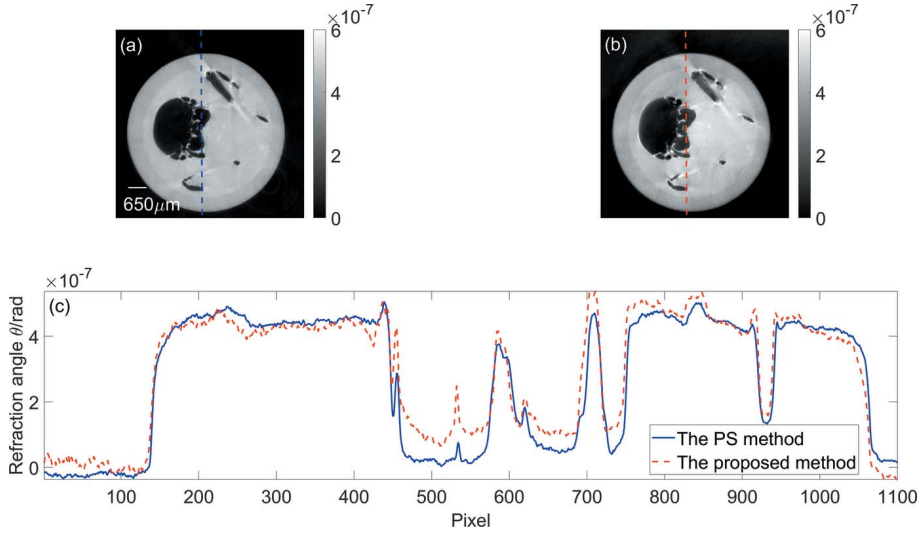

Figure 10
Reconstructed phase slices of a bee by (*a*) the PS method and (*b*) the proposed method, as well as (*c*) their profiles comparison as the dotted line in panels (*a*) and (*b*).

feasibility. To a great extent, the proposed method combines the advantages of the high efficiency of the reverse projection method and the universal applicability of the PS method.

We compared the proposed method with the PS method rather than the original reverse projection method, because the original reverse projection method did not work in the case considered here. Furthermore, the scattering signal was neglected in the proposed method, but the good agreements of the results in experiment between the two methods have demonstrated its feasibility and validity in the case of non-

uniform reference. We believe it would be used widely in fast and dose-constrained imaging, which is required in biological and medical imaging.

APPENDIX A
Derivation of equation (14)

From equation (8),

$$T = \frac{I_F}{I_R} = a_F\left\{1 + V_F \cos\left[2\pi\frac{x_g^0 + d\theta}{p_2} + \varphi_F\right]\right\} \Big/ a_R\left\{1 + V_R \cos\left[2\pi\frac{x_g^0 - d\theta}{p_2} + \varphi_R\right]\right\},$$

we can derive

$$Ta_R + Ta_R V_R \cos\left[2\pi\frac{x_g^0 - d\theta}{p_2} + \varphi_R\right] = a_F + a_F V_F \cos\left[2\pi\frac{x_g^0 + d\theta}{p_2} + \varphi_F\right]. \quad (25)$$

Then

$$Ta_R + Ta_R V_R \cos\left[2\pi\frac{x_g^0}{p_2} + \varphi_R\right]\cos\left(\frac{2\pi d}{p_2}\theta\right) + Ta_R V_R \sin\left[2\pi\frac{x_g^0}{p_2} + \varphi_R\right]\sin\left(\frac{2\pi d}{p_2}\theta\right) = a_F + a_F V_F \cos\left[2\pi\frac{x_g^0}{p_2} + \varphi_F\right]\cos\left(\frac{2\pi d}{p_2}\theta\right) - a_F V_F \sin\left[2\pi\frac{x_g^0}{p_2} + \varphi_F\right]\sin\left(\frac{2\pi d}{p_2}\theta\right). \quad (26)$$

Defining the following equations,

$$A_{F/R} = a_{F/R} V_{F/R} \cos\left[2\pi\frac{x_g^0}{p_2} + \varphi_{F/R}\right], \quad (27)$$

$$B_{F/R} = a_{F/R} V_{F/R} \sin\left[2\pi\frac{x_g^0}{p_2} + \varphi_{F/R}\right]. \quad (28)$$

Equation (26) is simplified to be

$$Ta_R + TA_R \cos\left(\frac{2\pi d}{p_2}\theta\right) + TB_R \sin\left(\frac{2\pi d}{p_2}\theta\right) = a_F + A_F \cos\left(\frac{2\pi d}{p_2}\theta\right) - B_F \sin\left(\frac{2\pi d}{p_2}\theta\right). \quad (29)$$

If $A_F - TA_R \neq 0$ or $B_F + TB_R \neq 0$, equation (29) yields

$$\frac{A_F - TA_R}{\left[(A_F - TA_R)^2 + (B_F + TB_R)^2\right]^{1/2}}\cos\left(\frac{2\pi d}{p_2}\theta\right) - \frac{B_F + TB_R}{\left[(A_F - TA_R)^2 + (B_F + TB_R)^2\right]^{1/2}}\sin\left(\frac{2\pi d}{p_2}\theta\right) = \frac{-a_F + Ta_R}{\left[(A_F - TA_R)^2 + (B_F + TB_R)^2\right]^{1/2}}. \quad (30)$$

With definition of the following equations,

$$\cos(\beta) = \frac{A_F - TA_R}{\left[(A_F - TA_R)^2 + (B_F + TB_R)^2\right]^{1/2}}, \quad (31)$$

$$\sin(\beta) = \frac{B_F + TB_R}{\left[(A_F - TA_R)^2 + (B_F + TB_R)^2\right]^{1/2}}, \quad (32)$$

$$\cos(\gamma) = \frac{-a_F - Ta_R}{\left[(A_F - TA_R)^2 + (B_F + TB_R)^2\right]^{1/2}}, \quad (33)$$

we can obtain the critical equation (34), *i.e.* equation (14) in the main body of the paper,

$$\cos\left(\frac{2\pi d}{p_2}\theta + \beta\right) = \cos(\gamma). \quad (34)$$

Acknowledgements

The authors thank the staff of the BL13W1 beamline of Shanghai Synchrotron Radiation Facility for providing help in the experiments.

Funding information

This work was partly supported by the National Natural Science Foundation of China (NSFC 11805205, U1532113, 11475170), the National Key Research and Development Program of China (2017YFA0402904), the National Key Scientific Instrument and Equipment Development Projects of China (CZBZDYZ20140002), and the Fundamental Research Funds for the Central Universities (Grant No. PA2020GDKC0024).

References

Bech, M., Jensen, T. H., Feidenhans'l, R., Bunk, O., David, C. & Pfeiffer, F. (2009). *Phys. Med. Biol.* **54**, 2747–2753.
Bevins, N., Zambelli, J., Li, K., Qi, Z. H. & Chen, G. H. (2012). *Med. Phys.* **39**, 424–428.
Bravin, A., Coan, P. & Suortti, P. (2013). *Phys. Med. Biol.* **58**, R1–R35.
Chen, G. H., Zambelli, J., Li, K., Bevins, N. & Qi, Z. H. (2011). *Med. Phys.* **38**, 584–588.
David, C., Nöhammer, B., Solak, H. H. & Ziegler, E. (2002). *Appl. Phys. Lett.* **81**, 3287–3289.
Epple, F. M., Pfeiffer, F., Ehn, S., Thibault, P., Koehler, T., Potdevin, G., Herzen, J., Pennicard, D., Graafsma, H. & Noel, P. B. (2015). *IEEE Trans. Med. Imaging*, **34**, 816–823.
Fu, J., Shi, X. H., Guo, W. & Peng, P. (2019). *Sci. Rep.* **9**, 1113.
Ge, Y. S., Li, K., Garrett, J. & Chen, G. H. (2014). *Opt. Express*, **22**, 14246–14252.
Gromann, L. B., Bequé, D., Scherer, K., Willer, K., Birnbacher, L., Willner, M., Herzen, J., Grandl, S., Hellerhoff, K., Sperl, J. I., Pfeiffer, F. & Cozzini, C. (2016). *Biomed. Opt. Expr.* **7**, 381–391.
Hagen, C. K., Endrizzi, M., Diemoz, P. C. & Olivo, A. (2016). *J. Phys. D Appl. Phys.* **49**, 255501.
Huang, Z., Kang, K., Li, Z., Zhu, P., Yuan, Q., Huang, W., Wang, J., Zhang, D. & Yu, A. (2006). *Appl. Phys. Lett.* **89**, 041124.
Li, P. Y., Zhang, K., Bao, Y., Ren, Y. Q., Ju, Z. Q., Wang, Y., He, Q. L., Zhu, Z. Z., Huang, W. X., Yuan, Q. X. & Zhu, P. P. (2016). *Opt. Express*, **24**, 5829–5845.
Marschner, M., Birnbacher, L., Mechlem, K., Noichl, W., Fehringer, A., Willner, M., Scherer, K., Herzen, J., Noël, P. B. & Pfeiffer, F. (2016). *Opt. Express*, **24**, 27032–27045.

Marschner, M., Willner, M., Potdevin, G., Fehringer, A., Noël, P. B., Pfeiffer, F. & Herzen, J. (2016). *Sci. Rep.* **6**, 23953.
Momose, A., Kawamoto, S., Koyama, I., Hamaishi, Y., Takai, K. & Suzuki, Y. (2003). *Jpn. J. Appl. Phys.* **42**, L866–L868.
Momose, A., Yashiro, W., Maikusa, H. & Takeda, Y. (2009). *Opt. Express*, **17**, 12540–12545.
Pelliccia, D., Rigon, L., Arfelli, F., Menk, R. H., Bukreeva, I. & Cedola, A. (2013). *Opt. Express*, **21**, 19401–19411.
Pfeiffer, F., Bech, M., Bunk, O., Kraft, P., Eikenberry, E. F., Brönnimann, C., Grünzweig, C. & David, C. (2008). *Nat. Mater.* **7**, 134–137.
Pfeiffer, F., Kottler, C., Bunk, O. & David, C. (2007). *Phys. Rev. Lett.* **98**, 108105.
Pfeiffer, F., Weitkamp, T., Bunk, O. & David, C. (2006). *Nat. Phys.* **2**, 258–261.
Tapfer, A., Bech, M., Pauwels, B., Liu, X., Bruyndonckx, P., Sasov, A., Kenntner, J., Mohr, J., Walter, M., Schulz, J. & Pfeiffer, F. (2011). *Med. Phys.* **38**, 5910–5915.
Tapfer, A., Bech, M., Velroyen, A., Meiser, J., Mohr, J., Walter, M., Schulz, J., Pauwels, B., Bruyndonckx, P., Liu, X., Sasov, A. & Pfeiffer, F. (2012). *Proc. Natl Acad. Sci. USA*, **109**, 15691–15696.
Wang, M., Zhu, P. P., Zhang, K., Hu, X. F., Huang, W. X., Cen, Y. W., Yuan, Q. X., Yu, X. L. & Wang, J. Y. (2007). *J. Phys. D Appl. Phys.* **40**, 6917–6921.
Wang, Z. L., Gao, K., Chen, J., Ge, X., Zhu, P. P., Tian, Y. C. & Wu, Z. Y. (2012). *Chin. Phys. B*, **21**, 118703.
Wei, W. B., Wu, Z., Wei, C. X., Hu, Y., Liu, G. & Tian, Y. C. (2017). *Proc. SPIE*, **10255**, 102551O.
Wen, H., Bennett, E. E., Hegedus, M. M. & Rapacchi, S. (2009). *Radiology*, **251**, 910–918.
Wu, Z., Gao, K., Chen, J., Wang, D. J., Wang, S. H., Chen, H., Bao, Y., Shao, Q. G., Wang, Z. L., Zhang, K., Zhu, P. P. & Wu, Z. (2015). *Med. Phys.* **42**, 741–749.
Wu, Z., Gao, K., Wang, Z., Ge, X., Chen, J., Wang, D., Pan, Z., Zhang, K., Zhu, P. & Wu, Z. (2013). *Med. Phys.* **40**, 031911.
Wu, Z., Gao, K., Wang, Z., Wei, C., Wali, F., Zan, G., Wei, W., Zhu, P. & Tian, Y. (2018). *J. Synchrotron Rad.* **25**, 1222–1228.
Wu, Z., Gao, K., Wang, Z. L., Shao, Q. G., Hu, R. F., Wei, C. X., Zan, G. B., Wali, F., Luo, R. H., Zhu, P. P. & Tian, Y. C. (2017). *J. Appl. Phys.* **121**, 213102.
Xi, Y., Kou, B., Sun, H., Qi, J., Sun, J., Mohr, J., Börner, M., Zhao, J., Xu, L. X., Xiao, T. & Wang, Y. (2012). *J. Synchrotron Rad.* **19**, 821–826.
Yashiro, W. & Momose, A. (2015). *Opt. Express*, **23**, 9233–9251.
Zanette, I., Bech, M., Pfeiffer, F. & Weitkamp, T. (2011). *Appl. Phys. Lett.* **98**, 094101.
Zanette, I., Bech, M., Rack, A., Le Duc, G., Tafforeau, P., David, C., Mohr, J., Pfeiffer, F. & Weitkamp, T. (2012). *Proc. Natl Acad. Sci. USA*, **109**, 10199–10204.
Zhu, P. P., Zhang, K., Wang, Z. L., Liu, Y. J., Liu, X., Wu, Z., McDonald, S. A., Marone, F. & Stampanoni, M. (2010). *Proc. Natl Acad. Sci. USA*, **107**, 13576–13581.